Main S/T results / foregrounds

Objective 1 - Numerical optimization for a low noise subsonic jet pump (WP1)

The objective was achieved through a RANS CFD analysis of a set of candidate solutions. First, a number of candidate geometries were defined. The set consisted in seven cases with various lengths of the primary jet pipe, of which three cases with shorter lengths (1D, 2D and 3D) and four cases with longer pipes (1D, 2D, 3D and 4D), two cases with chevrons, one with an angle between chevrons of 55° and one with 90°; and one case with fluidics. The 10 candidate solutions, together with the baseline, are summarized below:

- Case 0: Baseline case
- Case 1: 55° degrees chevron
- Case 2: 90° degrees chevron case
- Case 3: 1 D longer diameter case
- Case 4: 2 D longer diameter case
- Case 5: 3 D longer diameter case
- Case 6: 4 D longer diameter case
- Case 7: 1 D shorter diameter case
- Case 8: 2 D shorter diameter case
- Case 9: 3 D shorter diameter case
- Case 10: Fluidic injection

For the first nine candidate solutions, the RANS numerical the test cases were set up, the computational domain was defined and discretized and the proper boundary conditions were imposed. Once all this was done, than numerical simulation has been performed for each of the geometries mentioned above. Finally, the result analysis was performed and the best suited geometries for the project requirements were identified. The results, summarized in Table 1, indicated that from the efficiency point of view the best solution is case 3. The results in Table 1 are normalized with respect to the baseline measured values, provided by the Task Leader.

Table 1 - Performances of the candidate solutions

	Mass flow inlet 1	Mass flow inlet 2	Mass flow outlet	Efficiency	Q2/Q1
Baseline	0.941	1.000	0.986	0.314	3.275
Chevrons 55 degrees (Lchev)	0.974	0.998	0.992	0.294	3.06
Chevrons 90 degrees (Schev)	0.988	1.010	1.006	0.317	3.152
1D shorter	0.929	1.027	1.003	0.290	3.4
2D shorter	0.926	1.066	1.032	0.297	3.54
3D shorter	0.926	1.082	1.044	0.299	3.6
1 D longer	0.935	0.958	0.952	0.306	3.16
2 D longer	0.935	0.927	0.929	0.301	3.06
3 D longer	0.932	0.886	0.898	0.288	2.93
4 D longer	0.929	0.851	0.870	0.282	2.82

From the entrainment point of view, as seen in Figure 1, the best solution is case 9 (3 diameters shorter than baseline case, Figure 2), closely followed by case 8 (2 diameters shorter than baseline case, Figure 3).
However, the results analysis shows that high levels of turbulence kinetic energy are observed in case 9, which will affect in turn the acoustic performances of the jet pump. From the turbulent kinetic energy levels standpoint (shown in Figure 4 at two diameters from the jet nozzle), the best solution, if we look at turbulent kinetic energy levels, is case 7 (one diameter shorter than baseline, Figure 5), again closely followed by case 8.
Based on these results, the best, first selected solution is case 8, as a compromise between the entrainment and the acoustic criteria, with the 90 degree chevrons (see Figure 3 and Figure 4).
Considering the two chevron cases 1 (Figure 6) and 2 (Figure 7), the best solution is the 90° chevron case (case 2), from the point of view of turbulent kinetic energy levels, axial velocity, vorticity, entrainment and efficiency.

Consequently, the 2D shorter primary pipe solution will be tested, both experimentally and numerically, using LES, with (optimized solution 1.2) and without 90° (optimized solution 1.1) chevrons.

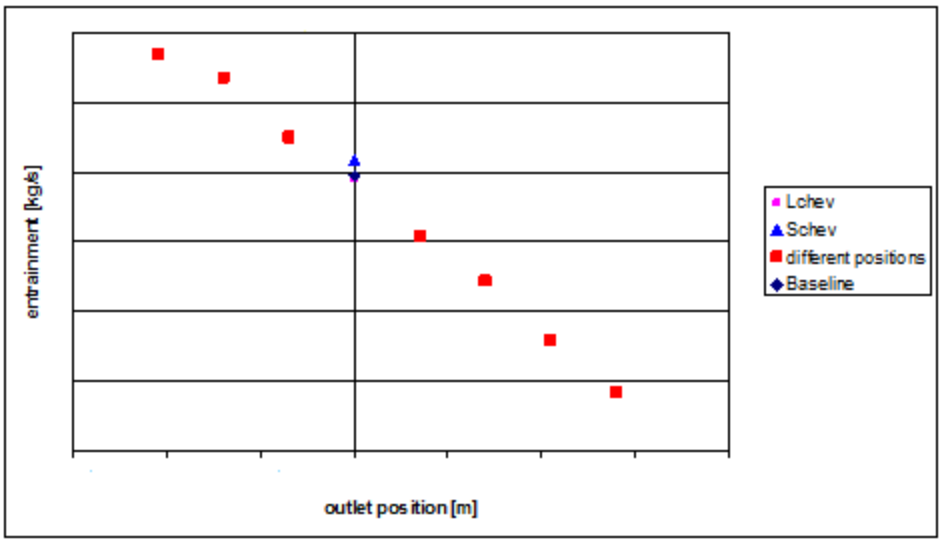

Figure 1. Entrained mass flow at X= 0.414 m, upstream of the primary jet pipe outlet

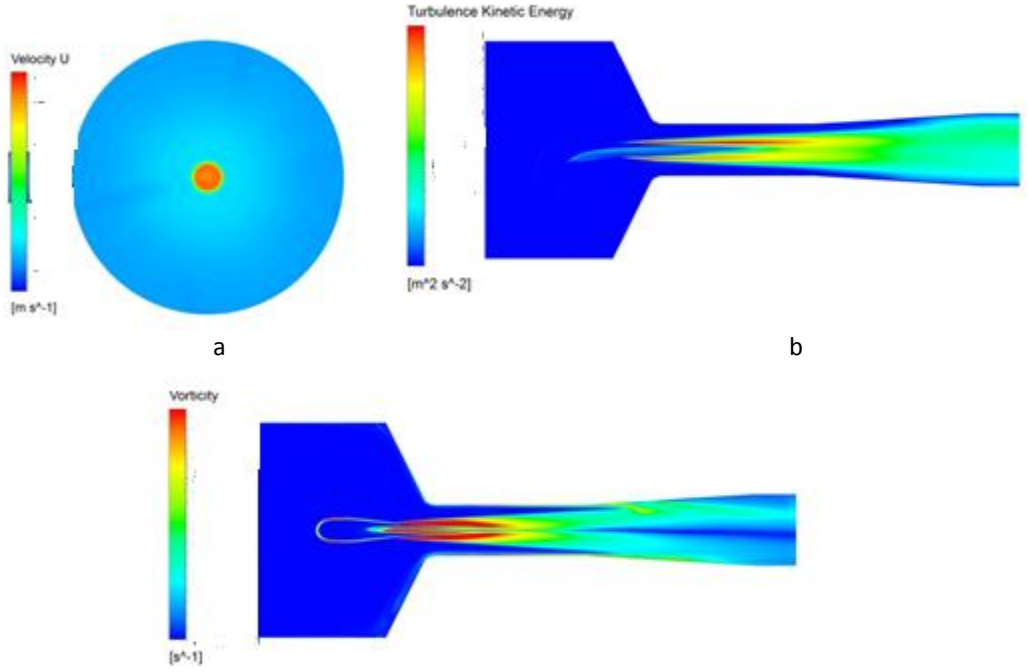

a b

c

Figure 2. Case 9: a) Axial velocity in the YZ plane at one diameter from the inlet; b) Turbulent kinetic energy in the XZ plane; c) Vorticity in the XY plane

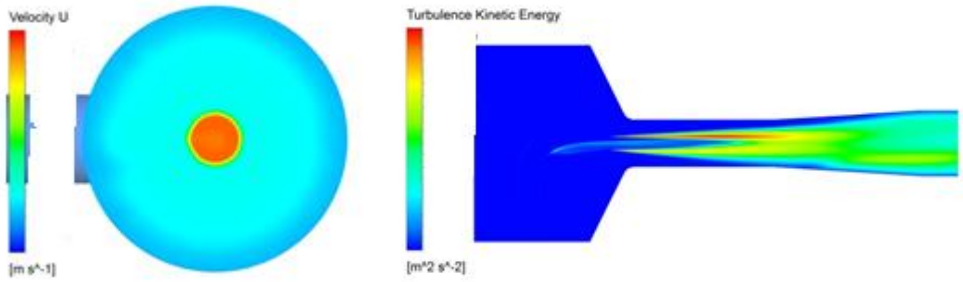

a b

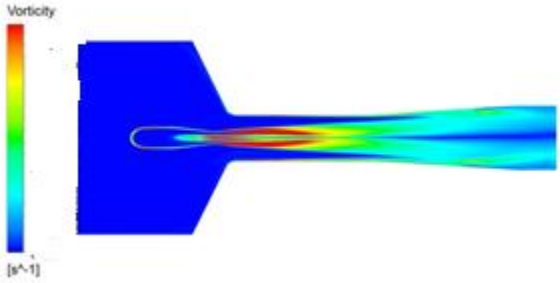

c

Figure 3. Case 8: a) Axial velocity in the YZ plane at one diameter from the inlet; b) Turbulent kinetic energy in the XZ plane; c) Vorticity in the XY plane

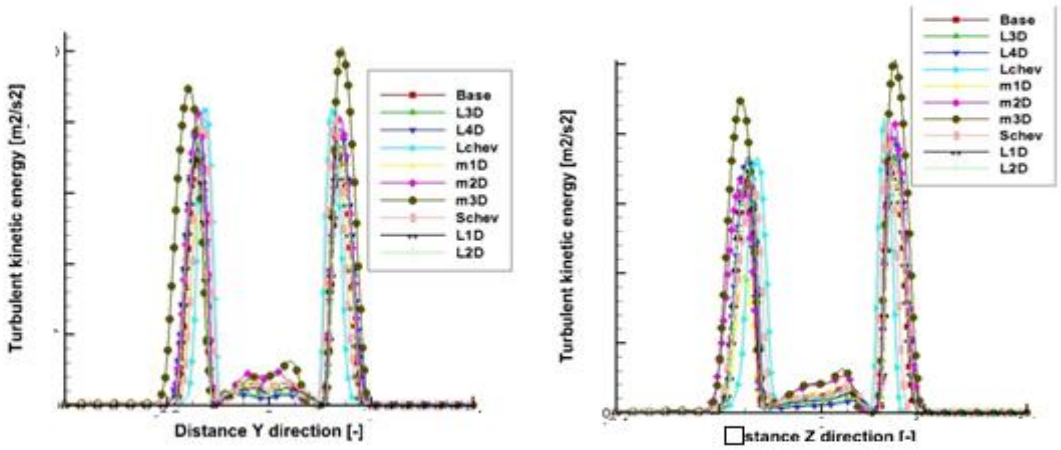

Figure 4. Turbulent kinetic energy at two diameters from the outlet. Lengths normalized by mixing diameter

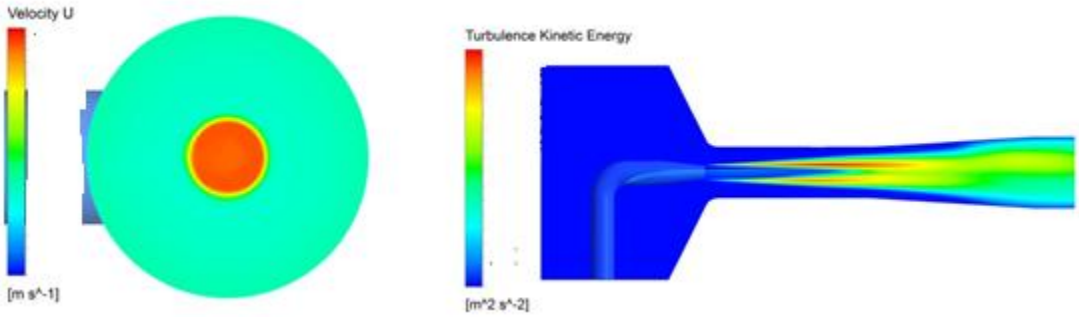

a b

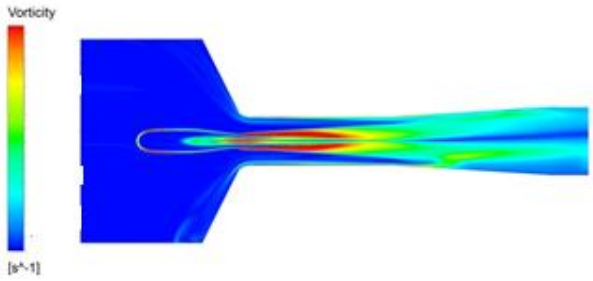

C

Figure 5. Case 7: a) Axial velocity for YZ plane at one diameter from the inlet; b) Turbulent kinetic energy for XZ plane; c) Vorticity for the XY plane

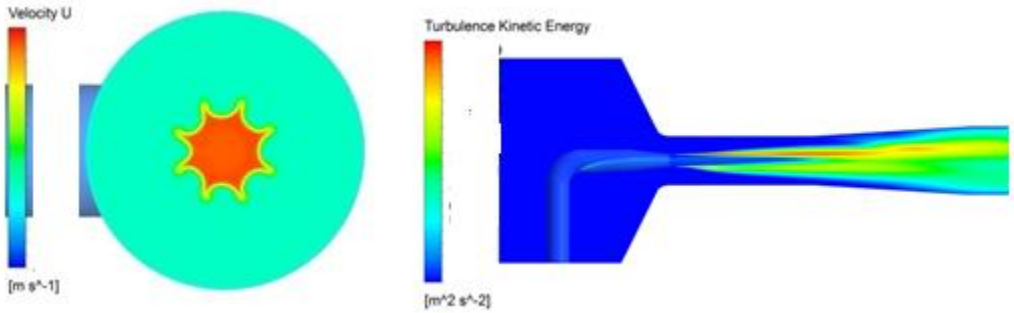

a b

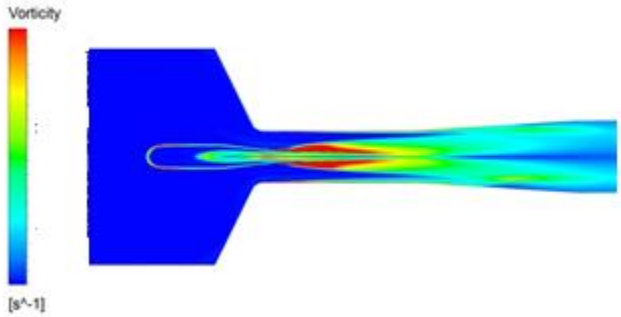

c

Figure 6. Case 1: a) Axial velocity for YZ plane at one diameter from the inlet; b) Turbulent kinetic energy for XZ plane; c) Vorticity for the XY plane

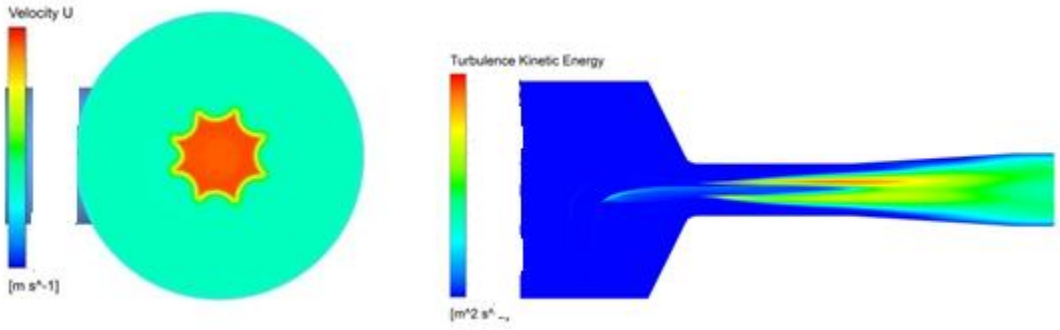

a b

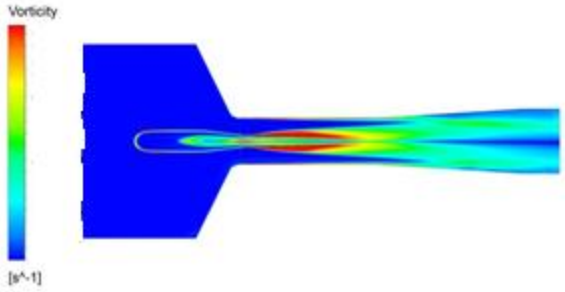

c

Figure 7. Case 2: a) Axial velocity for YZ plane at one diameter from the inlet; b) Turbulent kinetic energy for XZ plane; c) Vorticity for the XY plane

The 10th candidate solution, namely the fluidic injection, the following considerations apply:
It can be noted, based on the RANS results, that the primary jet pipe creates blockage and is a source for decreasing entrainment. Hence, alternate solutions able to decrease loss have been sought. Such an approach is to use many small nozzles around the outer circumference of the centred entrained flow. With this approach, a back flow region in the mid at the centre axis of the mixing channel is generated. With a shape optimization of the channel walls the back flow may be reduced, but not eliminated. However, driving the flow by injecting the stream from the side walls does not cause a direct drag penalty. A vast variety of possible configurations can be optimized to achieve optimal entrainment. The optimization parameters are the injection angle, the number of injectors and the diameter of the injection pipes. However, the difficulty increases with the operating range of application, since a configuration optimal one operation condition might not be ideal for another operation set point. During the first WP of the project, the above working principle was proven by a chosen geometry for the baseline operation condition, which can be optimized in later stages.
For jet in crossflow the penetration depth was investigated as a function of the velocity ratio. However, for this setup the jets from the channel walls are required to drive the flow. Thus, the jets need to be declined towards the intended flow direction.
A steep injection angle leads to deep penetration into the channel mid. However, only a low momentum is transferred and the obtained flow velocities and therefore the mass-flow at the channel exit would be low. Additionally, the jets streams might meet in the centerline of the channel, where the mixing leads to flow against the desired flow direction.
On the other hand, a shallow angle would cause high losses on the walls and the mixing of the two fluids is expected to intense. The number of injectors determines the initial interface area between the primary and the secondary stream. A high number of injectors lead to an increased area exposed to the mixing and a high injector number distributes the primary fluid more equally in the channel. However, small jets defuse faster in the secondary stream and are less beneficial for the momentum transport.
Considering the above, a fluidic configuration has been proposed and numerically tested through LES simulation. The proposed constructive solution is presented in Figure 8 and uses eight pipes placed on the circumference, pointing towards the channel axis have been used. The pipes are inclined at an angle of 25° towards the intended streaming direction in the channel. For the operation condition described at baseline, the primary jet exhausting the pipe is close to choke conditions at the exit of the pipe. To achieve a similar mass-flow at with injection from the channel walls, the area of the exit pipe shall be conserved. Based on this observation, a diameter of 12 mm has been chosen for technological reasons. Due to the slightly smaller area (less than 5 %), a proportionally smaller mass-flow rate is expected compared to the baseline. Also for technological reasons, the pipe centre was placed one pipe diameter downstream of the baseline primary pipe exit. The boundary conditions described in the previous section have been applied. Hence, the total pressure and total temperature imposed at the primary jet have been used as inlet condition for all the pipes on the channel walls. The flow direction has been set normal to the inlet boundary. The jet pipe length has been chosen to be about two pipe diameters. The jets are thought to be fed by a plenum surrounding the injection pipes, which distributes the pressure among the pipes.

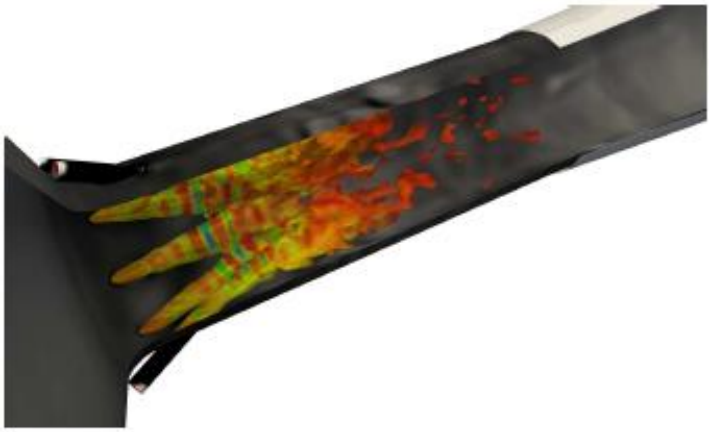

Figure 8. Fluidic injection solution used for the LES numerical simulation. The jet structure is illustrated by an iso contour of the Mach-number, coloured by the static pressure.

Since the optimization potential of this solution was estimated as very high, and since the complexity of the flow is, in this case, significantly higher than for the previously considered cases, the numerical simulation of the fluidic injection case was, from the beginning, carried out using the LES approach.
The calculated mass-flow rate at the injectors is 0.306 kg/s, which corresponds to a slightly lower (about 5 %) mass-flow rate as for the primary stream of the baseline configuration.

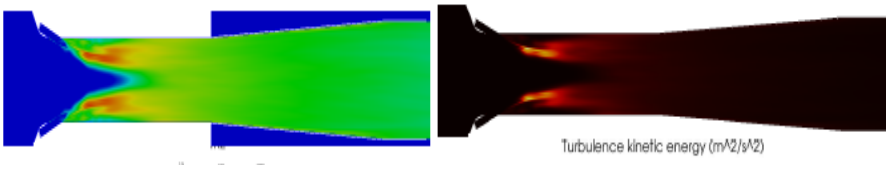

Figure 9. Turbulent kinetic energy contours on a linear (left) and logarithmic (right) scale.

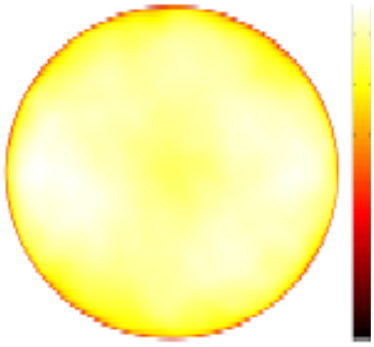

Figure 10. Time-averaged velocity magnitude contours.

The turbulence kinetic energy distribution is shown in Figure 9. High amplitudes are dominant in the region where the hanging vortices form and where strong shedding of the hairpin vortices occurs. With the disruption of the vortical structures, the turbulence kinetic energy levels decrease to rather low equal distributed values. However, with this approach no shedding behind a pipe lip occurs and therefore the turbulence kinetic energy levels exhibit rather low peak values compared to the baseline configuration.
At the outlet of the jet pump a rather homogeneous velocity profile along the radius develops. However, a circular increase in velocity is observed in Figure 10, which stems the jets forming an annular ring-like flow shape.
Based on the above presented numerical results, the fluidic injection solution was selected for further numerical and experimental testing, as the second optimized solution (OS2)

Objective 2 – Design and manufacturing of the jet pump demonstrators (WP2)

In order to carry out the planned acoustic and aerodynamic experimental measurements for the baseline solution (BS) and the selected Optimized Solutions (OS), jet pump demonstrators have been designed and manufactured.
Based on the WP 1 findings the prototype mechanical designs for the baseline and the optimized solutions were performed. The assembly and manufacturing drawings for the baseline and the two selected optimized solutions were finalized. The design of the optimized solutions aimed for a modular approach, parts of the optimized geometries making use of some of the baseline components, in order to minimize costs and time. The CAD models are presented in Figure 11 (BS), Figure 12 (OS1), and Figure 13 (OS2). The assembly drawings are presented, respectively, in Figures 14 – 16, and the detail drawings of the two different nozzles for OS1.1 and OS 1.2 are presented in Figures 17 and 18.
The baseline demonstrator assembly was designed to facilitate access to different parts. This is necessary because parts of this demonstrator can be changed to obtain the optimized geometry one or two. This solution is more efficient than to make a different demonstrator for each optimized geometry.
The OS1 demonstrator is derived from the baseline solution, but the primary jet nozzle exit is placed upstream of the baseline primary jet nozzle exit, at a distance of two nozzle diameters. The demonstrator parts are the same as for the baseline demonstrator, only the mounting of the 90° bend segment inside the cylindrical segment 1 varies.
Two variants of this solution will be manufactured and tested, one with a classic nozzle (OS1.1), and the other one with a 90° chevrons nozzle (OS1.2).

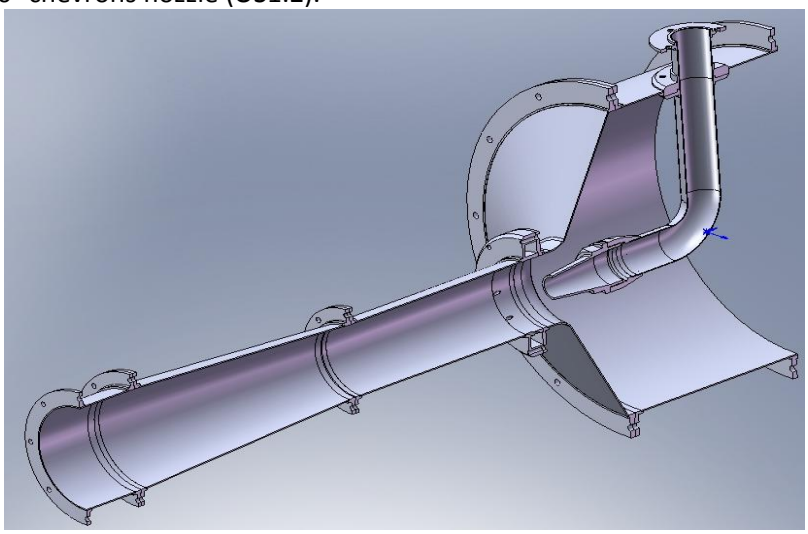

Figure 11. CAD model of the baseline

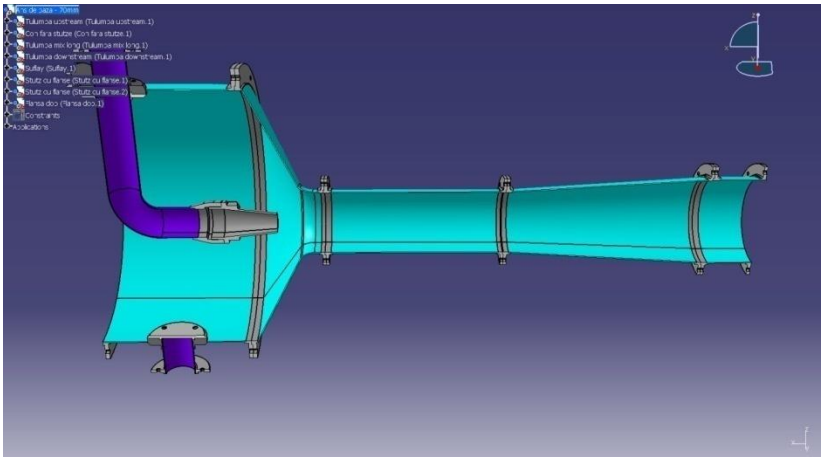

Figure 12. CAD model of the first optimized solution

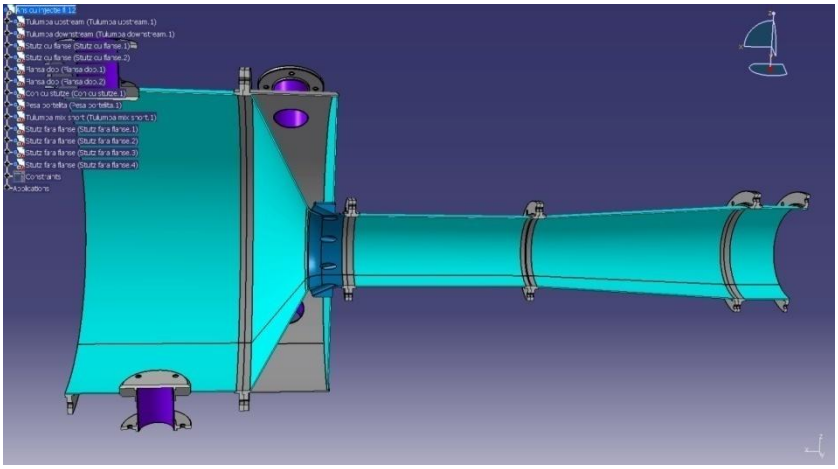

Figure 13. CAD model of the second optimized solution

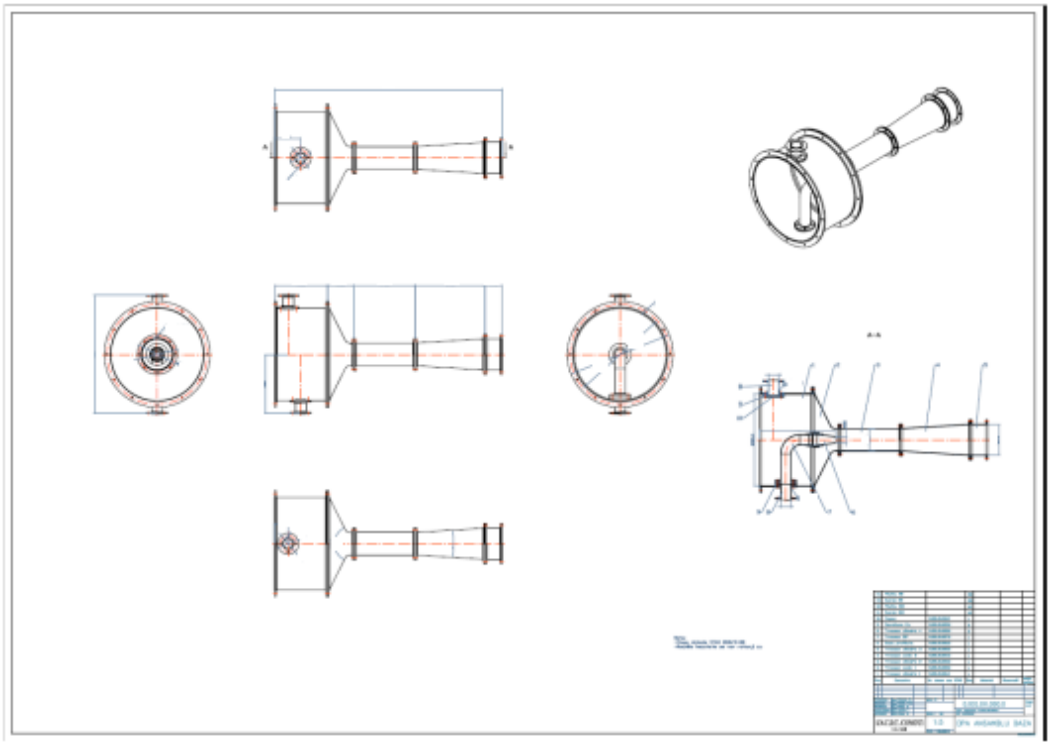

Figure 14. Baseline demonstrator assembly

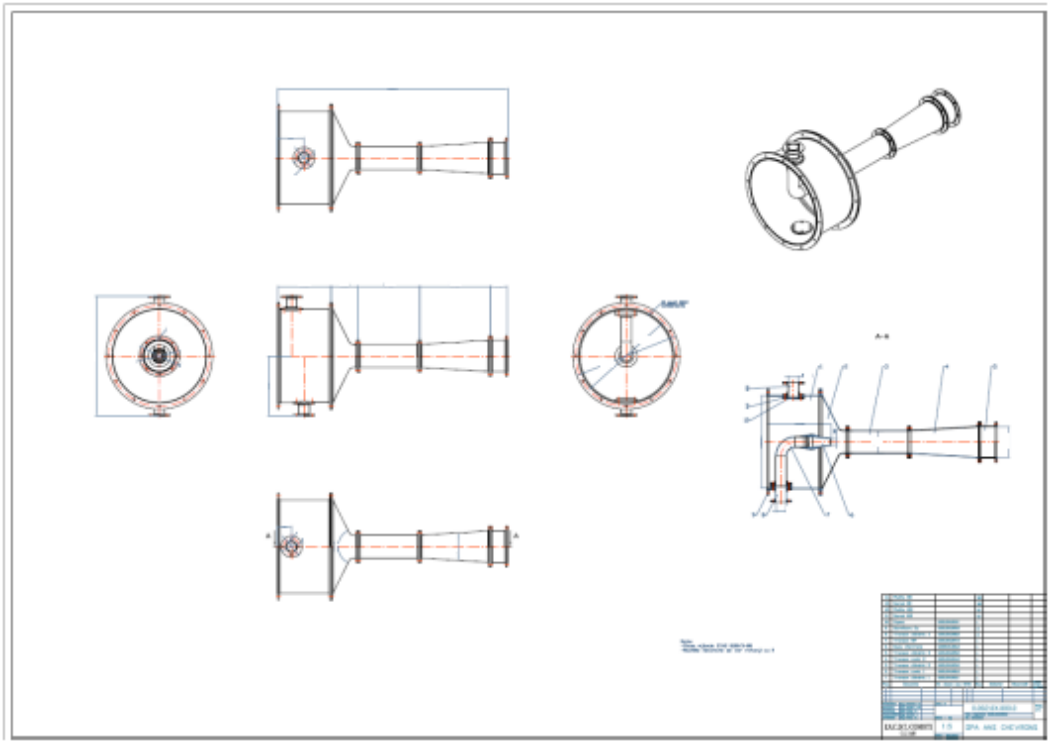

Figure 15. OS1 demonstrator assembly

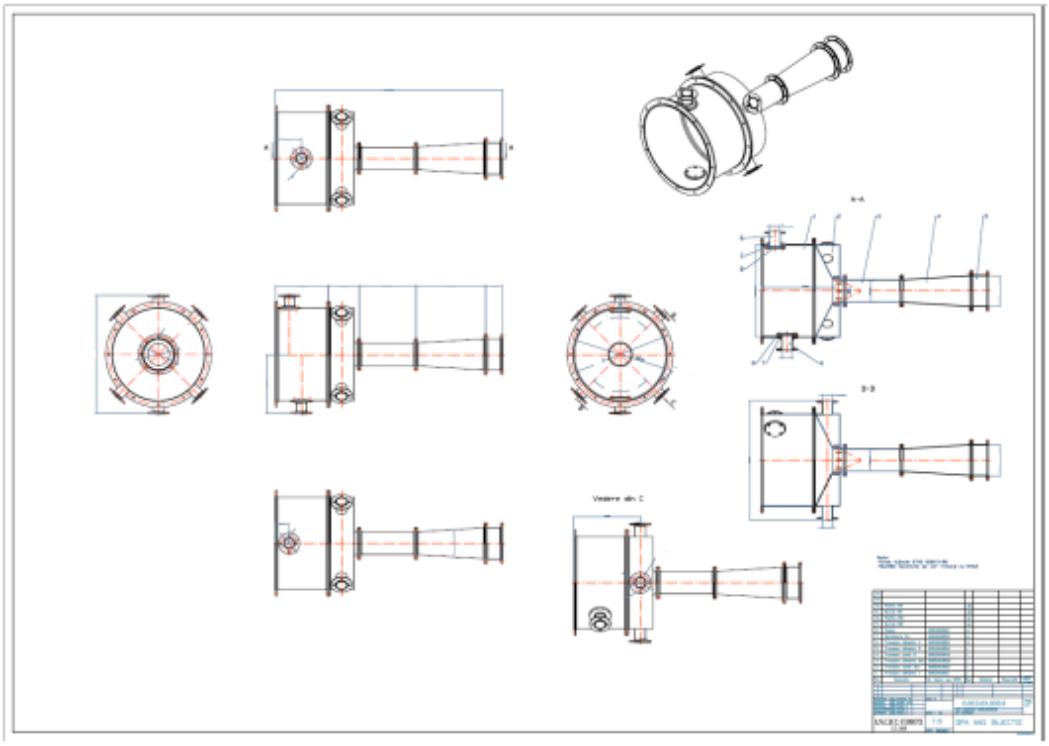

Figure 16. OS2 demonstrator assembly

The OS2 demonstrator uses the fluidic injection concept, applied on the same baseline body configuration. The solution uses eight injectors equally spaced on the jet pump casing, injecting the air

at 25° with respect to the jet pump centerline.

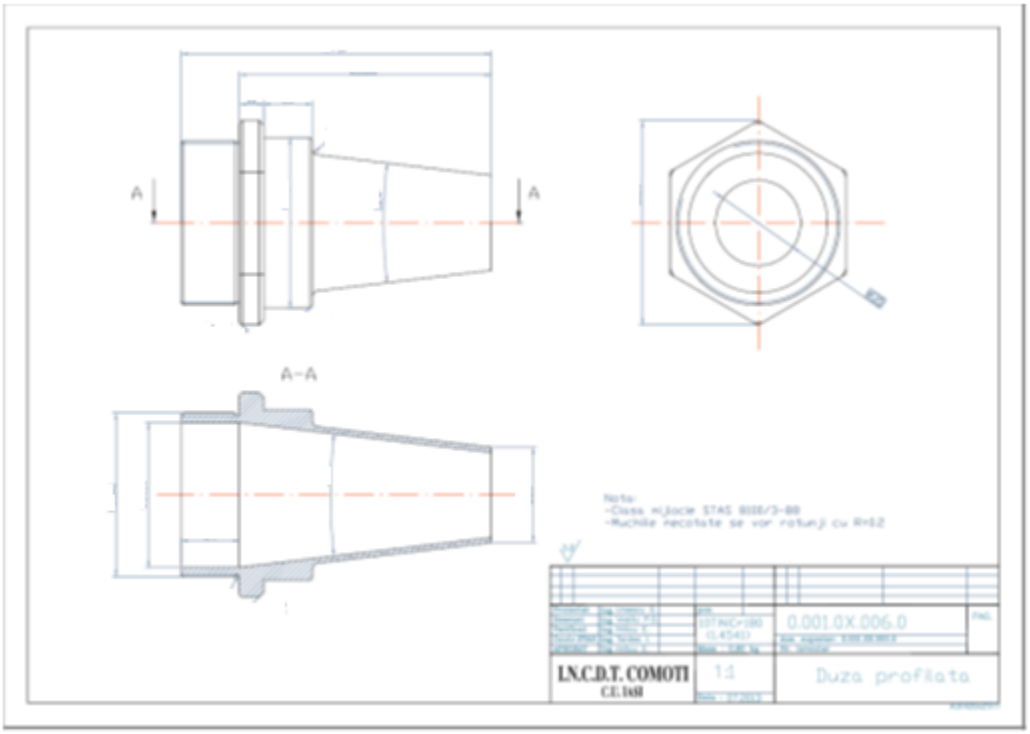

Figure 17. Classic nozzle

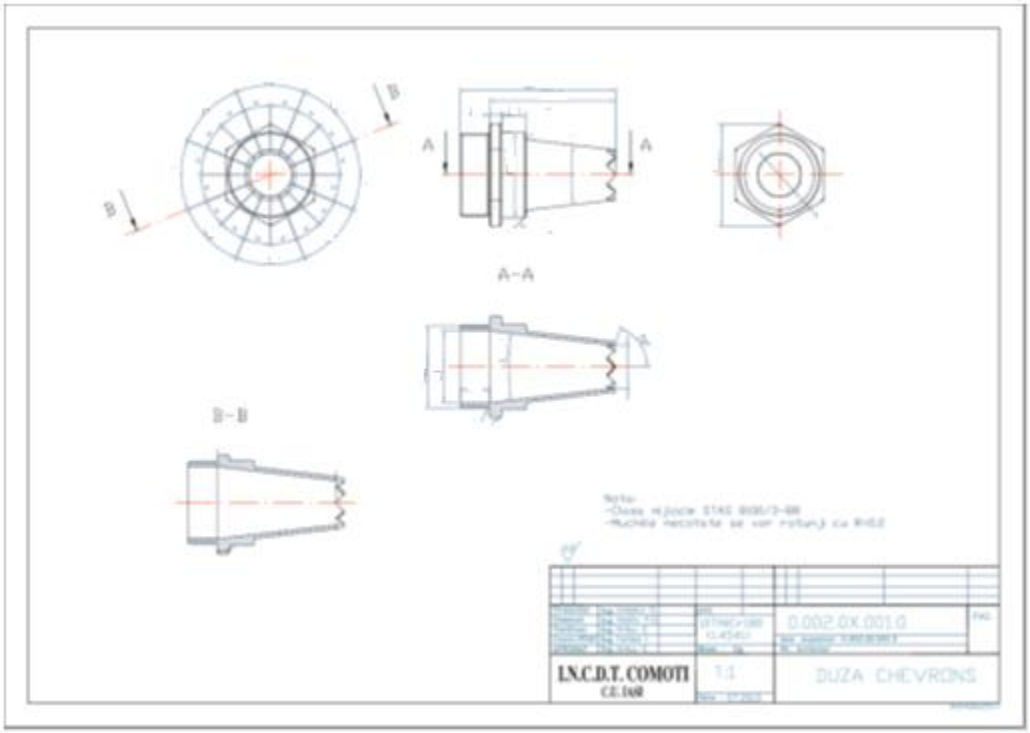

Figure 18. Chevrons nozzle

Based on these drawings, the jet pump demonstrators were manufactured. The manufactured parts are presented in Figure 19. Due to the modular design, the baseline solution and all the selected demonstrator solutions can be assembled from the manufactured parts presented below.

Figure 19. Manufactured demonstrators

Figure 20. Manufactured demonstrators

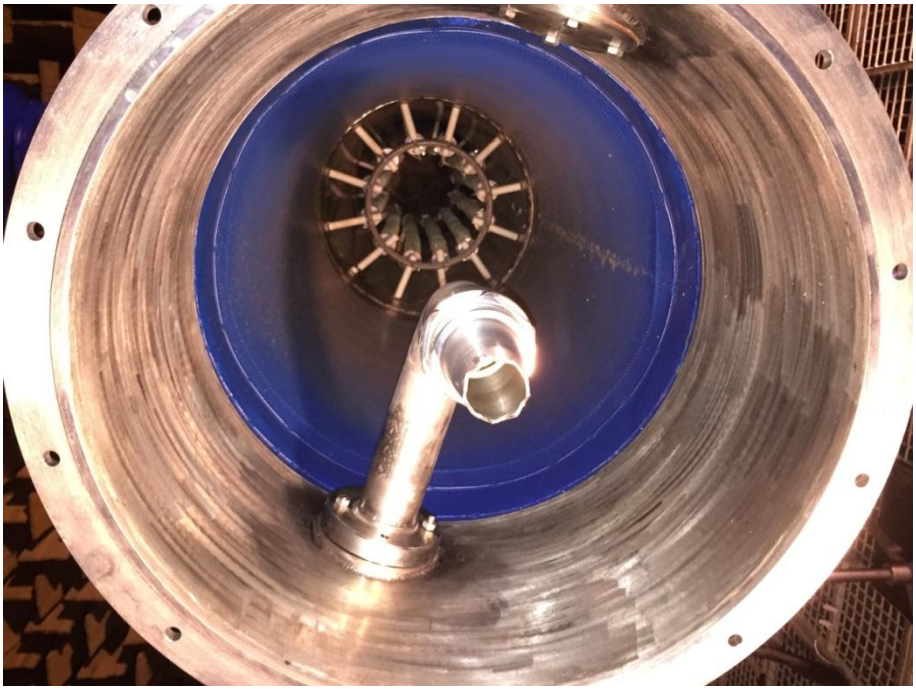

Figure 21. Manufactured demonstrators

The two different manufactured nozzles are presented in Figure 20 and Figure 21, assembled on the OS1.1, respectively OS1.2 demonstrators.

Objective 3 – Testing of the jet pump demonstrators (WP2)

Two sets of experimental measurements have been carried out in order to test the previously selected Optimized Solutions. The same measurements were carried out, for comparison purposes, on the Baseline Solution.
All the measurements throughout the project have been carried out under inlet conditions specified by the Task Leader.

Acoustic measurements were performed in the anechoic chamber at COMOTI. The following tests have been carried out during the acoustic experimental campaign:

Directivity tests

For evaluating the directivity, 6 microphones were used in the anechoic chamber. The microphones were positioned on a radius of 3m, at 150 distances between each other and at a height of 1.6 m. Directivity measurements were performed for each of the defined configurations.
The results are presented Figure 22 and Tables 2 and 3. The values are normalized by the value registered by the 90° place microphone on the BS. It can be seen that OS1.1 and OS1.2 are giving almost the same results, but present an improvement by comparison with BS. The best results were obtained for OS2, as already predicted by the numerical simulations. The improvements can easily be seen; the pattern is not just shifted towards the jet pump exit, but is presents a considerable decrease in noise level at 750, 900, 1050 and 1650. Conf. 1 represents BS, Conf. 2 – OS1.1, Conf. 3 – OS1.2, and Conf. 4 – OS2.
In order to quantify the noise reduction of the proposed solution the averaged sound pressure level was determine using the global sound level from the directivity microphones, according to ISO 3744:2009. The results are presented in Table 4. The results are presented in Table 5, normalized by the baseline value.

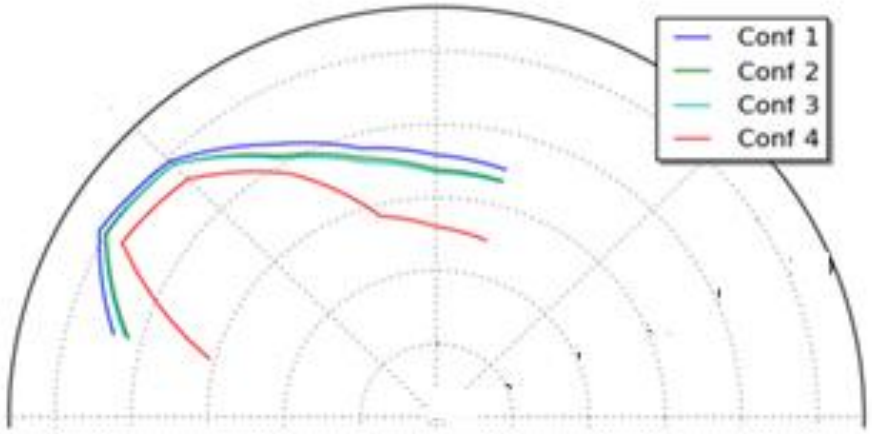

Figure 22. Directivity pattern for all tested configuration

Table 2. Recorded linear levels for each configuration during directivity measurements

No. mic	Position	BS	OS1.1	OS1.2	OS2
Mic 6	75grd	0.996	0.987	0.986	0.942
Mic 7	90grd	1.000	0.989	0.987	0.947
Mic 8	105grd	1.012	1.004	1.001	0.960
Mic 9	120grd	1.039	1.029	1.027	1.014
Mic 10	135grd	1.073	1.070	1.027	1.055
Mic 11	150grd	1.082	1.076	1.078	1.064
Mic 12	165grd	1.043	1.032	1.034	0.973

Table 3. Recorded A weighted levels for each configuration during directivity measurements

No. mic	Position	BS	OS1.1	OS1.2	OS2
Mic 1	3m	0.955	0.952	0.952	0.896
Mic 6	75grd	0.990	0.978	0.977	0.971
Mic 7	90grd	1.000	0.986	0.983	0.975
Mic 8	105grd	1.014	1.007	1.003	0.988
Mic 9	120grd	1.055	1.048	1.045	1.037
Mic 10	135grd	1.097	1.097	1.097	1.074
Mic 11	150grd	1.113	1.108	1.108	1.086
Mic 12	165grd	1.059	1.042	1.048	0.993

Table 4. Averaged sound pressure level for each configuration

Parameter	Configuration			
	BS	OS1.1	OS1.2	OS2
Averaged sound pressure level [dB]	1.000	0.994	0.994	0.973
Averaged sound pressure level - A weighted[dB(A)]	1.000	0.995	0.995	0.974
Sound reduction [dB]	-	-0.6	-0.6	-2.6
Sound reduction [dB(A)]	-	-0.5	-0.5	-2.5

Near field tests

a. Acoustic intensity

The acoustic intensity measurements were performed, according with ISO 9614 Part 3. The configuration used in the test area remained unchanged during tests. An area of 480 x 180 mm was overlaid on the jet pump area and a total of 24 cells (60x60mm) was considered. In each cell, the sound intensity was, and results are ploted and image overlaid on each tested element Figure 23. The acoustic intensity measurements were performed for all 4 configurations, on the established measurement grid, covering the mixing part.

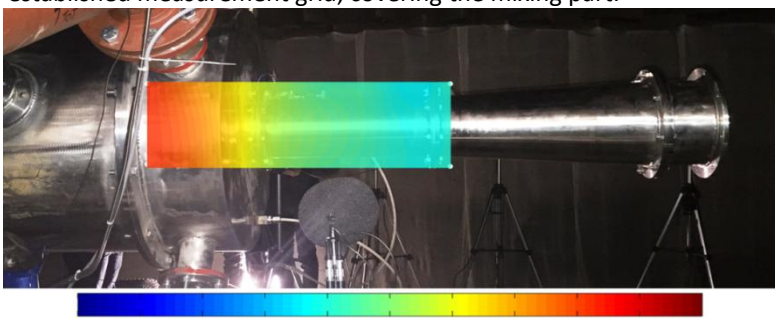

Figure 23. Measurement results overlaid on the measurement grid

As shown in Figure 24, the global sound intensity level cartography for BS and OS1 highlights that the outlet section has the greatest acoustic radiation, caused by the beginning of the turbulence flow. For the OS2 configuration (Figure 25), the inlet section and the injectors have the main acoustic radiation contribution.

From a global values point of view (Figure 26), OS1 can be identified as having a lower performance compared to BS. When looking into the frequency data, differences can be observed between OS1.1 and OS1.2 (Figure 27), especially in the 160 - 800Hz frequency range, where OS1.2 presents lower levels even with 3.7dB at 400Hz, (considered values measured at the centre line).

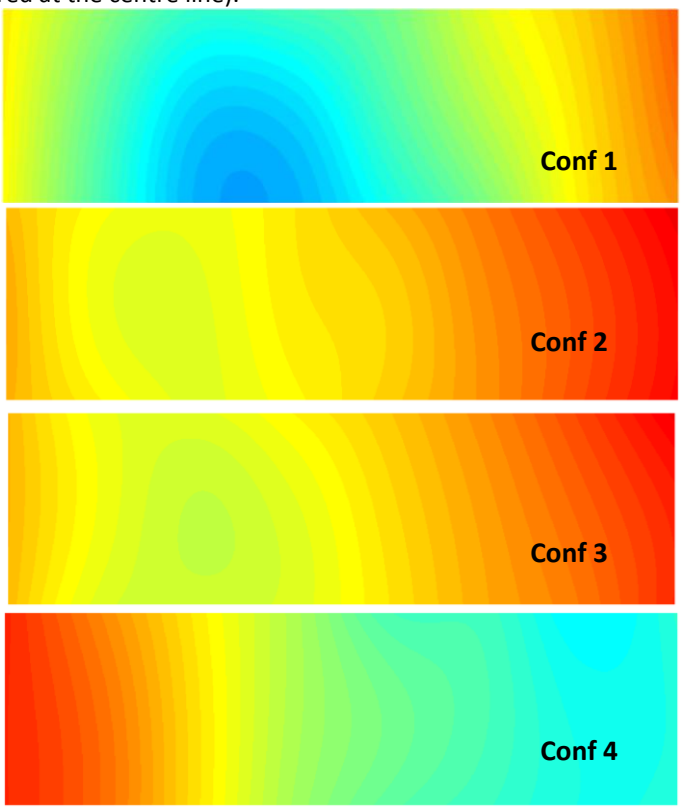

Figure 24. Intensity mapping - Global values obtained for all configurations

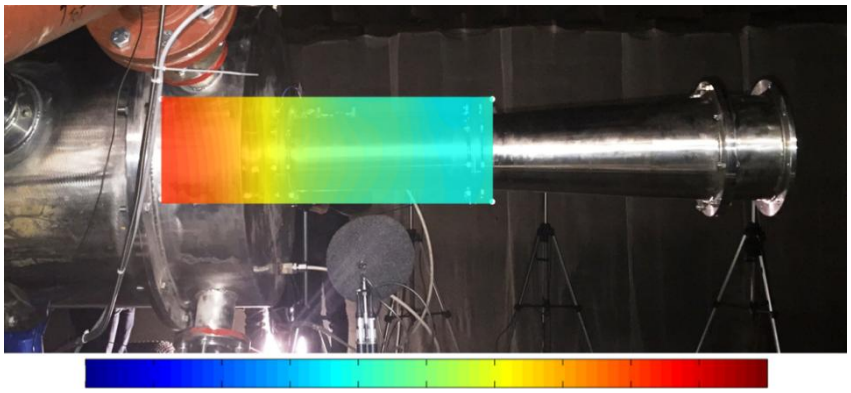

Figure 25. Intensity map for OS2

b. Inter-correlations

Four microphones were placed near the jet pump, positioned at a distance of 0.3 m from the pump, correlated with 4 accelerometers. One was positioned on the diffuser part, at the exit of the primary flow, two on the mixing part ~at a distance of 2D and 4D, and one in the near field of the mixing part, at a distance of 12D. All three distances are considered form the exit of the primary flow. These positions are correlated with the positions of the accelerometers for vibration measurements. A correlation coefficient is considered in the preliminary analysis. The correlation measurements were done using 4 microphones and 4 accelerometers. In Table 5, the global sound pressures for each microphone and for each tested configuration are presented. In Table 6, the vibration levels for each accelerometer are presented. The values are normalized by the 0D BS values.

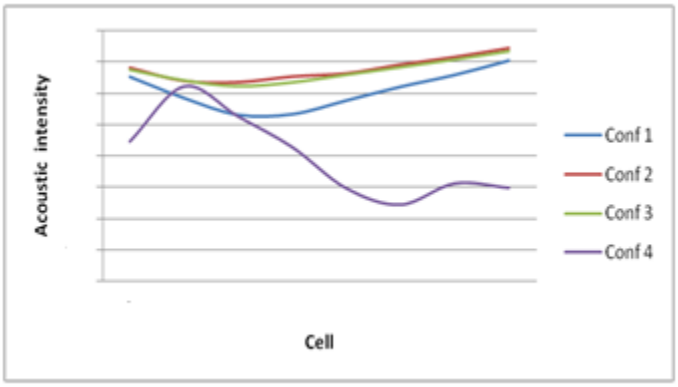

Figure 26. Acoustic intensity global levels recorded at central line of the measurement grid

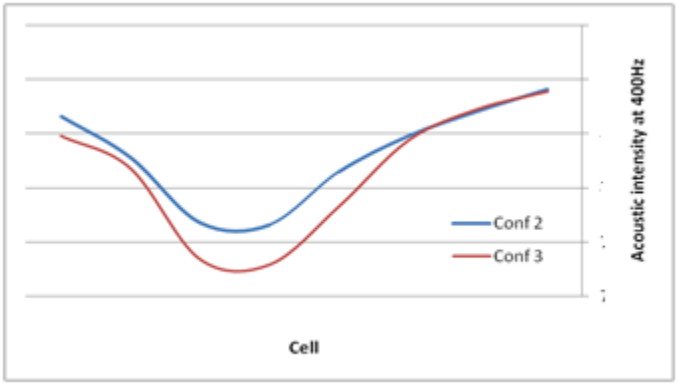

Figure 27. Acoustic intensity at 400Hz for OS1

Before the test, a natural modes test has been made for the pump section for BS. The results indicated the following natural frequencies: 450, 890, 1160, 1178, 1481, 1821Hz.

Table 5. Global sound pressure levels during intercorrelation measurements

Mic no. (Distance)	BS	OS1.1	OS1.2	OS2
Mic 2 (0D)	1.000	0.988	0.982	0.991
Mic 3 (2D)	1.000	0.991	0.986	0.986
Mic 4 (4D)	0.956	0.952	0.942	0.952
Mic 5 (12D)	1.027	1.034	1.017	0.945

Table 6. Vibration levels during intercorrelation measurements

Acc no.	BS (RMS)	OS1.1 (RMS)	OS1.2 (RMS)	OS2 (RMS)
Acc 1 (0D)	1.000	0.986	0.806	1.251
Acc 2 (2D)	1.118	1.080	0.895	2.904
Acc 3 (4D)	1.404	1.464	1.222	4.106
Acc 4 (12D)	1.298	1.160	1.014	2.069

In order to have a comparative analysis the vibration spectra for all configurations, in Figure 28 the spectra recorded by Acc. 1 are plotted. For Acc. 1 it can be observed that for BS and OS1, the vibration levels are low because of low turbulence levels in the core of the jet. For OS2, a broadband vibration from 1000Hz to 4000Hz can be observed, caused by the turbulence from the injectors. These turbulences produce a broad band vibration which excites a natural frequency at 1800Hz.
Vibration levels recorded by Acc. 2 and presented in Figure 29, show that the turbulence increases for all the configuration, while on OS2 other peaks appear (1131Hz, 1162Hz) representing other natural frequencies. Vibrations recorded by Acc. 3 increase, as shown in Figure 30, the natural frequencies of the pump-duct system can be observed for all the configurations. The peak from 1225Hz is increasing which can be related to the diameter of the injectors and the immersing angle. For Acc. 4, the vibration level decreases, as shown in Figure 31. Major peaks, at 450, 837, 893, 1487, 1800Hz, and corresponds to the natural modes of the pump can be observed. To observe the influence of the vibration in the acoustic signal, a correlation function has been calculated between the vibration and acoustic signal. The correlation function highlights the contribution of the high frequencies vibration in the sound signal; low frequency sounds are strictly generated by the air turbulence.

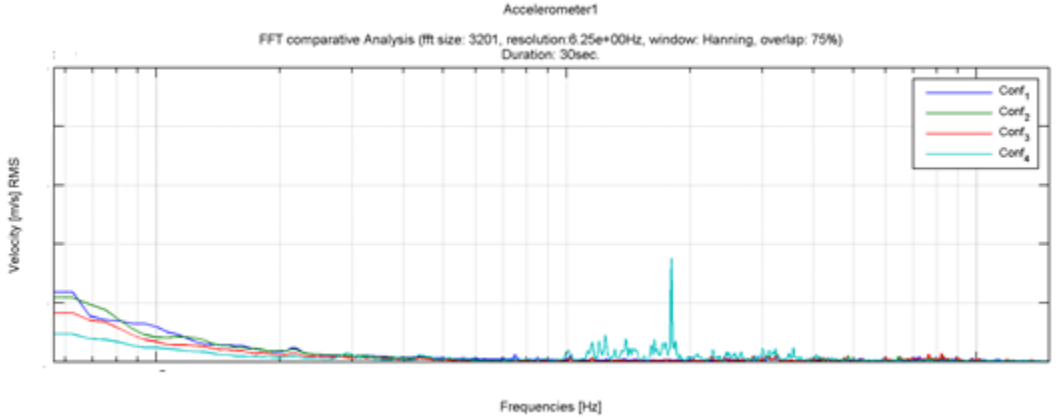

Figure 28. Comparative analysis of the vibration spectra in Acc1

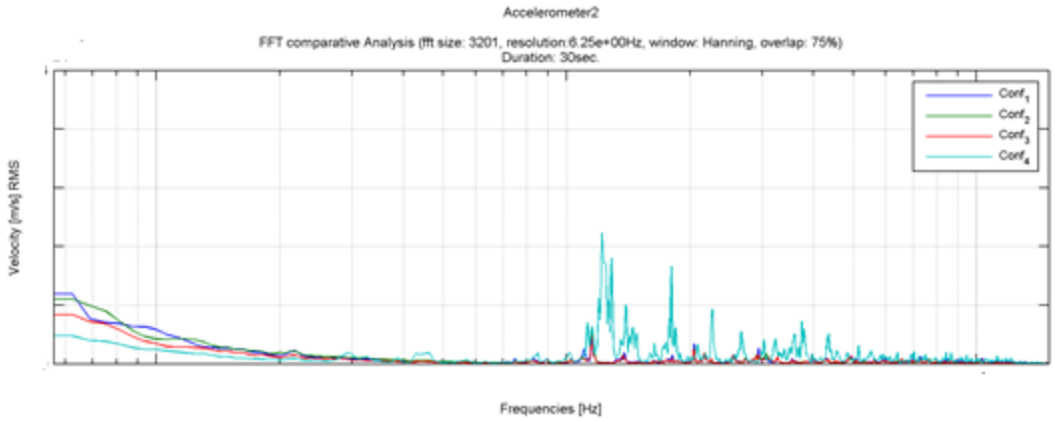

Figure 29. Comparative analysis of the vibration spectra in Acc2

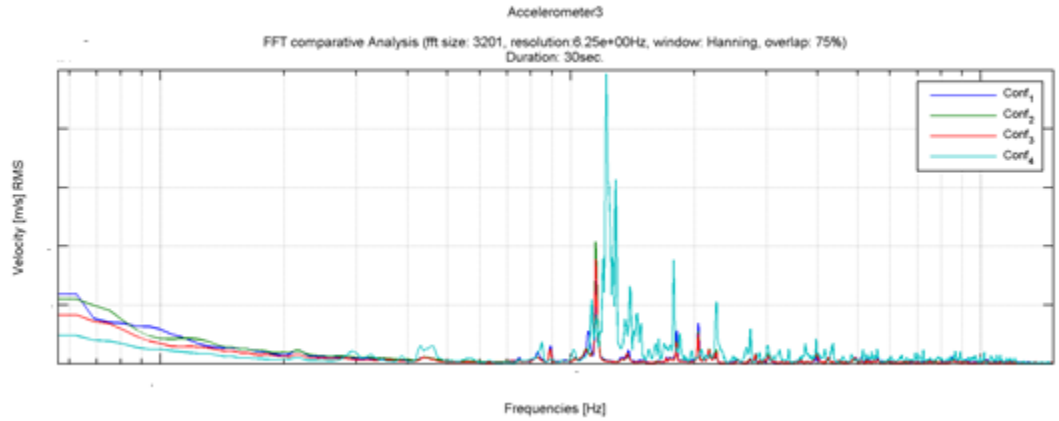

Figure 30. Comparative analysis of the vibration spectra in Acc3

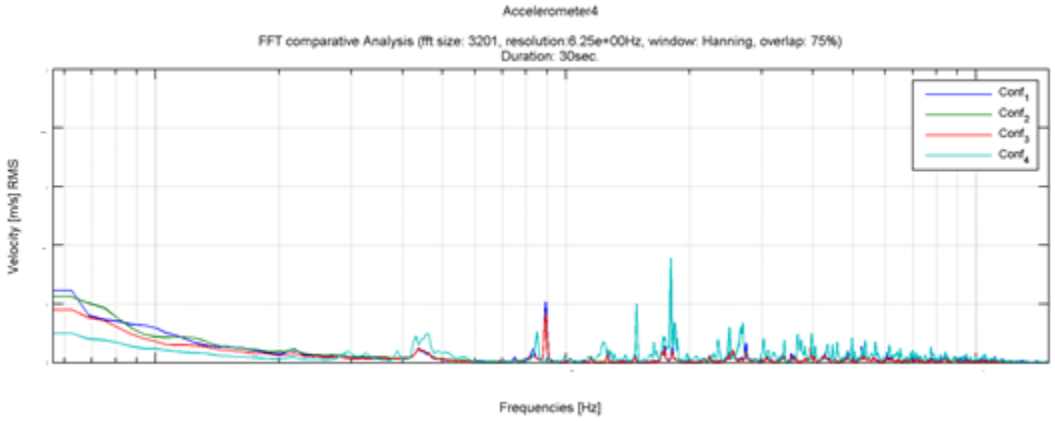

Figure 31. Comparative analysis of the vibration spectra in Acc4

Measurements at the silencer level

In order to observe the acoustic propagation on the secondary flow from the nozzle, the sound pressure level was measured on the secondary flow, at the silencer level, in one point, at a height of 3.7 m.
In the next figures a comparative analysis between mic 1 and mic 6 is presented in order to observe if there are acoustic influences from the secondary flow. For BS it can be observed that frequencies up from 400Hz are attenuated by the secondary flow; the low frequencies and the peak at 200 Hz representing the cut off frequency of the secondary flow duct. At the mic1 position of higher pressure

levels can be observed in Figure 32. For OS1.1, the cut off frequency of the second flow at around 200 Hz can be more clearly observed, in the mic 1 position. The translation of the nozzle produces an increasing of the low frequencies sound. This is caused by the fact that the inside translation makes the secondary flow enclosure to react more, as seen in Table 7. The values are normalized by the BS value at microphone 1 position.

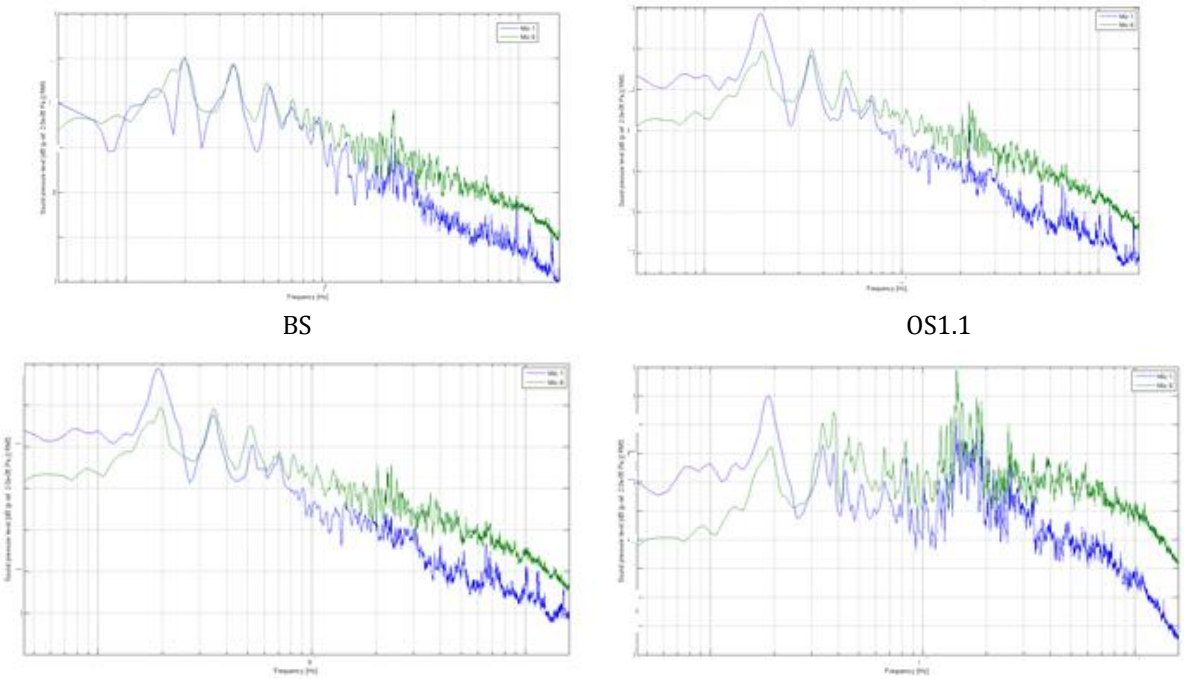

BS OS1.1

OS1.2 OS2

Figure 32. Comparative SPL analysis (mic 1 and 6)

Table 7. Recorded levels for each configuration during directivity measurements, in mic 1 and 6

No. mic	Position	BS [dB]	OS1.1 [dB]	OS1.2 [dB]	OS2 [dB]
Mic 1	3m	1.000	1.046	1.048	0.900
Mic 6	75 deg	1.019	1.010	1.009	0.964

Aerodynamic testing was carried out on the same four configurations. In order to provide the optical access to the experimental zone in the mixing region for the PIV measurements presented here, the cylindrical segment where the mixing of the primary and secondary air stream is occurring was replaced by a quartz tube of the same diameter. Since the quartz tube is not load bearing, a reinforcing system made up of several bars was designed, manufactured and installed in order to provide support for the demonstrator parts placed downstream of the experimental region. The measurement field for the PIV velocity measurements was a roughly rectangular domain placed in a horizontal plane along the baseline demonstrator centreline. The middle of the experimental field, marked with “x” in Figure 33, is placed at 1.386D, 2.386D, respectively 1.679D from the BS, OS1, and OS2 demonstrator primary air stream nozzle, along the demonstrator centreline.

After the stabilization of inlet thermodynamic parameters, 10 sets of 100 double images were captured by the ICCD cameras for post-processing in order to provide the instantaneous velocity fields.

The measurements results were presented with respect to an orthogonal, right, Cartesian coordinate system, as defined in Figure 33. For BS and OS 1, the angle of the measurement plane is of 20° relative to the radial duct of the demonstrator’s primary air stream. For OS2, the measurement plane contains

two diametrically opposed primary air inlet holes. This angle is denoted α in Figure 33, where the blue lines represent the coordinate system axes and the green rectangle represents the measurement field.
The mean, respectively the RMS velocity vector fields for all the studied configurations are presented in Figures 34 – 35, respectively 36 - 37.
The highest axial velocity component value on the centreline is measured for BS, while the lowest is measured for OS1, due to the axial distance to the primary exhaust nozzle. The fastest momentum mixing between the primary stream and the entrained air is registered for OS2, which is an advantage from the noise production standpoint. In the shear layer, large fluctuations of the mean axial velocity are observed, indicating a high level of turbulence in the region, with a maximum value noted for OS1.2, due to the presence of the chevrons. The tapering of the central air stream is found minimal for OS2, due to the configuration of the primary air inlet. Vortical structures are observed in the mean flow in the transversal and spanwise profiles, due to the detachment of the boundary layer on the mixing segment duct. The vortex is the strongest of OS2, due to the higher axial velocity gradients, and the weakest for both OS1 cases.
In the transversal direction, the axial velocity profile along the transversal direction is roughly parabolic for all the presented cases. The axial velocity is higher for the BS case, since the measurement section is the closest here to the primary jet nozzle exit. For all cases, the central, high velocity region of the flow expands towards downstream, due to the spreading of the primary jet. The spreading rate is slightly larger for OS1, with only marginal differences between the two nozzle shapes, and the smallest for OS2. The momentum mixing rate is roughly similar, with a slightly larger value registering for OS2. The transversal and spanwise velocity profiles indicate that the jet spreading is slightly higher in the central region for the BS, where the jet nozzle is closer, while the jet entrainment is more significant for OS1, due to the optimized geometry. The OS2 transversal and spanwise velocity profiles are different from the other cases, indicating a ring shaped jet that progresses radially towards the centreline as it moves downstream.

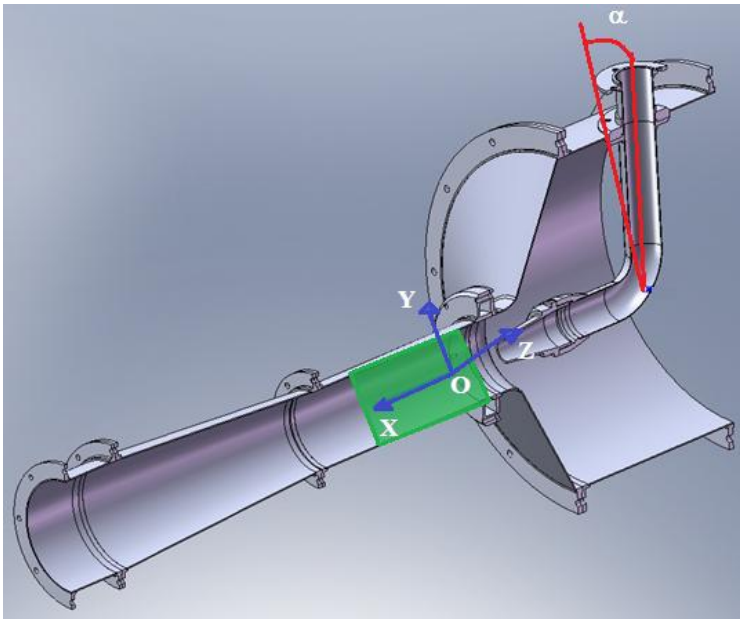

Figure 33. Coordinate system of the velocity measurements

The axial velocity fluctuation profiles are uniform in the upstream region, while far downstream outside of the jet, the turbulent fluctuation intensity decreases rapidly. For OS2, the axial velocity fluctuation profile presents an initial decay, follow by a sudden increase and the final decrease, at the same rate with the other cases. Overall, OS1 has the lowest RMS velocity in the axial direction, with OS1.1 being

the lowest in the near field, and OS1.2 the lowest in the far field. In the low intensity regions in the centre of the measurement field, OS 2 reaches the lowest RMS values.

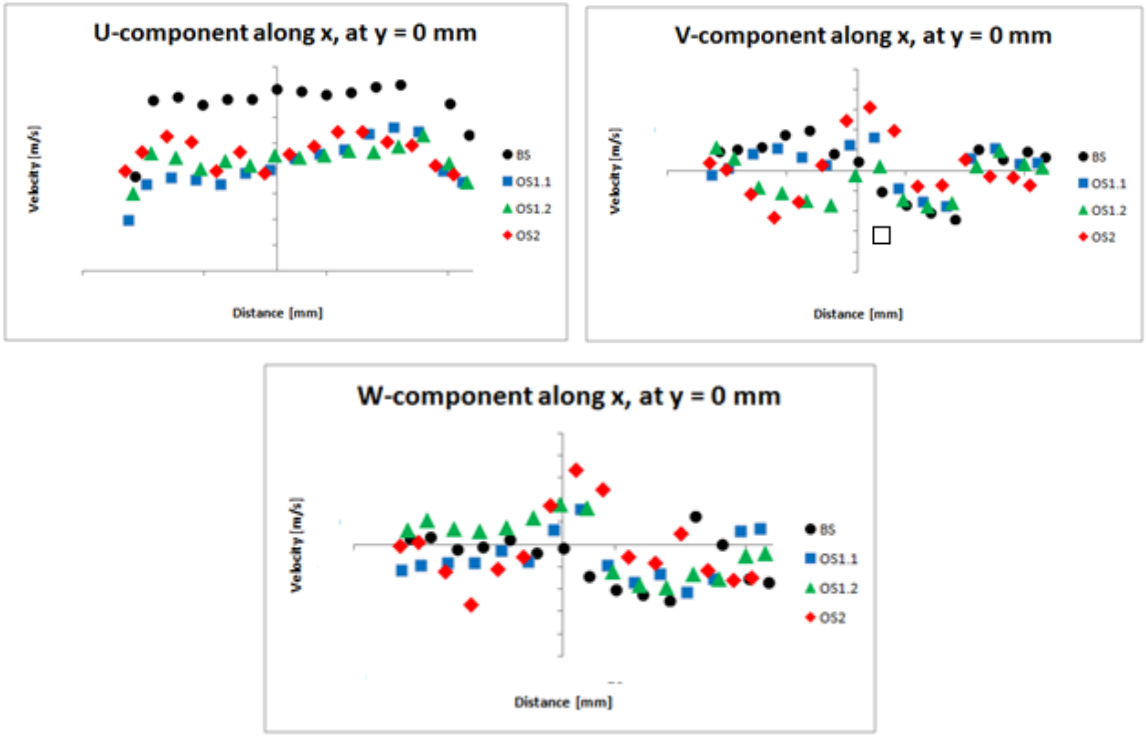

Figure 34. Mean velocity components along the x axis at y = 0 mm

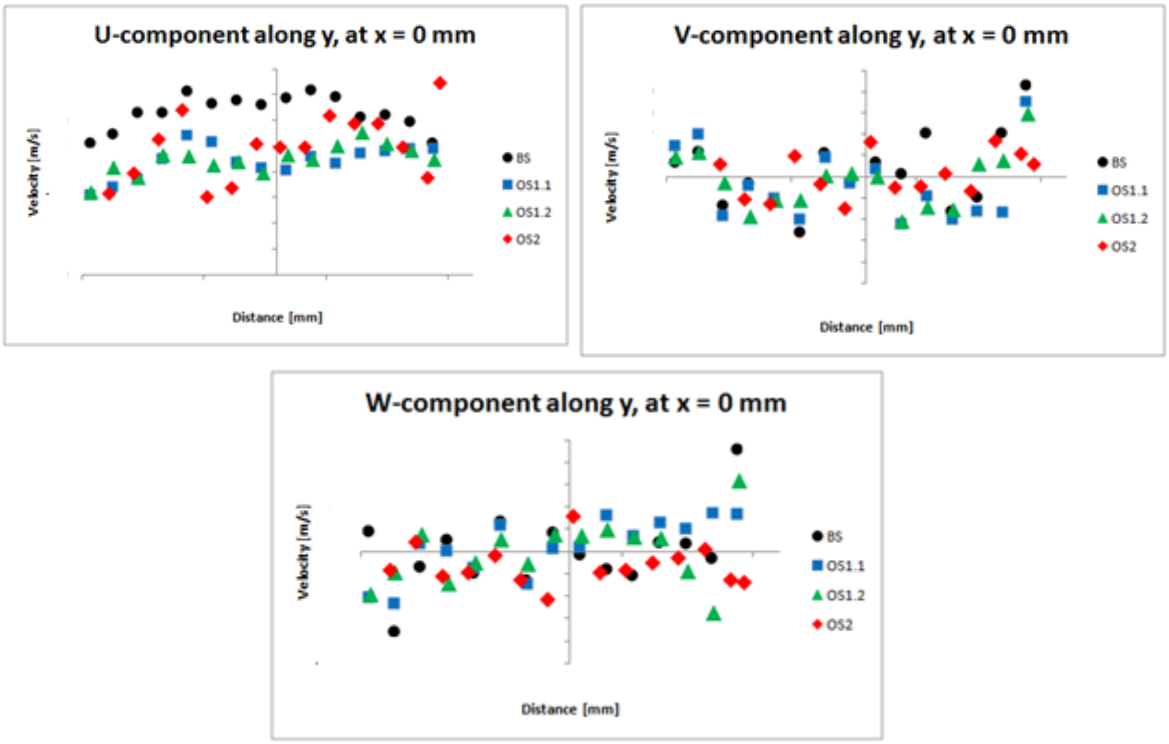

Figure 35. Mean velocity components along the x axis at y = 0 mm

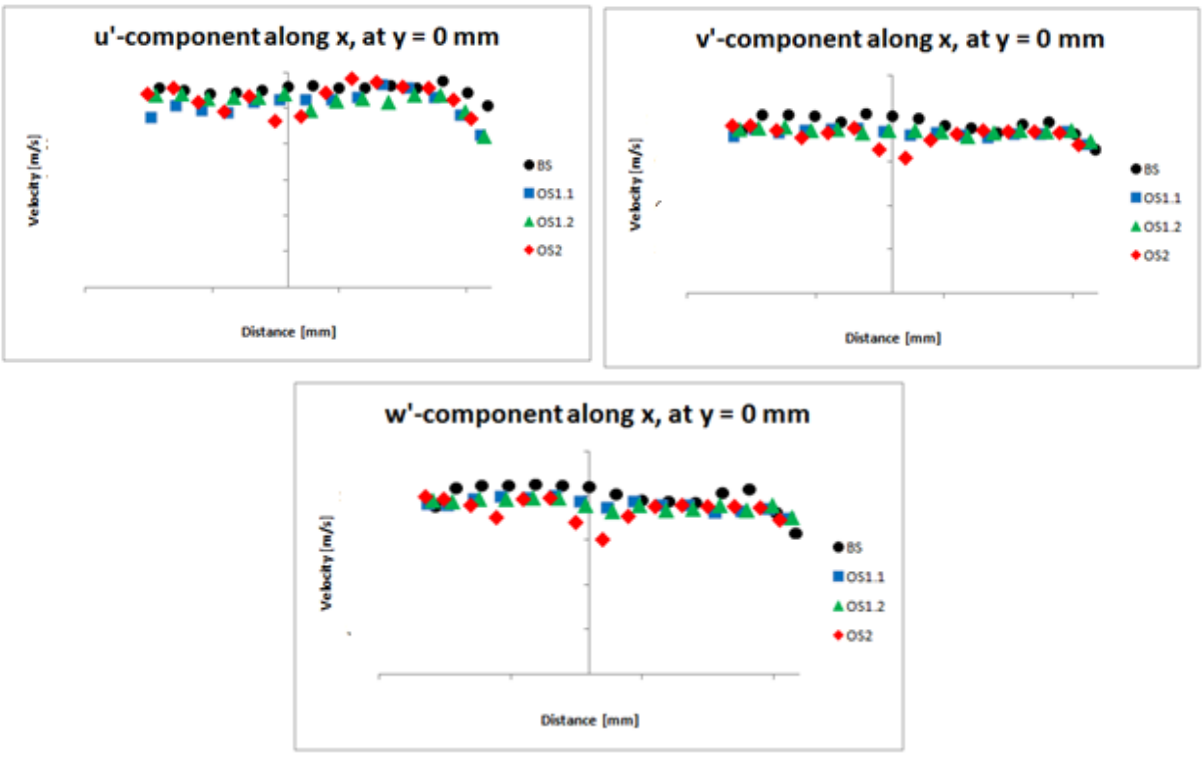

Figure 36. RMS velocity components along the x axis at y = 0 mm

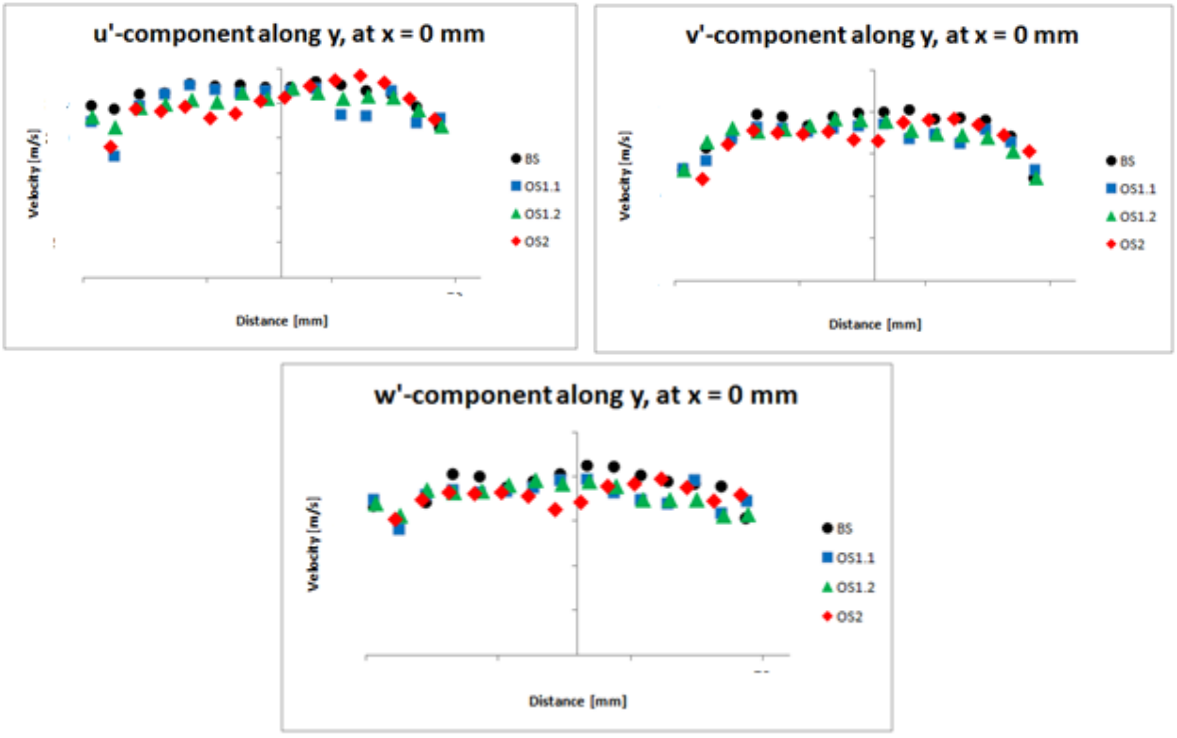

Figure 37. RMS velocity components along the y axis at x = 0 mm

In the shear layer region, all four profiles present a sudden increase, where the edge of the jet is crossed. The exit from the turbulent region of the shear layer triggers, far downstream, the decrease in

the RMS fluctuation intensity.
In the transversal and spanwise directions, the RMS fluctuation profiles are similar. At the centreline, BS and OS1 present a low value upstream region, corresponding to the jet potential core, for both non-axial velocity components. The sudden increase in the velocity fluctuations for both components occurs first for BS, than for OS1.2, and last for OS1.1, indicating that the length of the potential core increases in the same order. As in the axial velocity fluctuation case, the OS2 RMS profiles show two peaks. The BS RMS values are the highest, while OS2 provides the lowest RMS intensity in regions close to x = 0 mm.

Objective 4 - Unsteady simulations of a jet pump numerical simplified configuration (WP3)

The LES numerical simulations for the baseline and the selected optimized solutions have been carried out. A sample of the LES results is presented in Figure 38.
A modal flow decomposition method, i.e. DMD, was applied on the flow field data.
Turbulence is characterized by its three-dimensionality and inherent complex non-linear flow phenomena. The non-linear operator challenges conclusive interpretations of the chaotic flow-field appearance. However, the presents of coherent flow structures with over-imposed turbulence have been observed. The coherent flow structures characterize the flow behavior and are induced by the geometry constrains and the boundary conditions.
In order to extract the essential behavior of the flow via the coherent structures, modal flow decomposition can be performed. Thereby, the complexity of the non-linear operator is estimated by a low-order estimator representing the intrinsic properties of the flow. This less complex description is utilized for further investigation instead of the compressible Navier-Stokes equations.

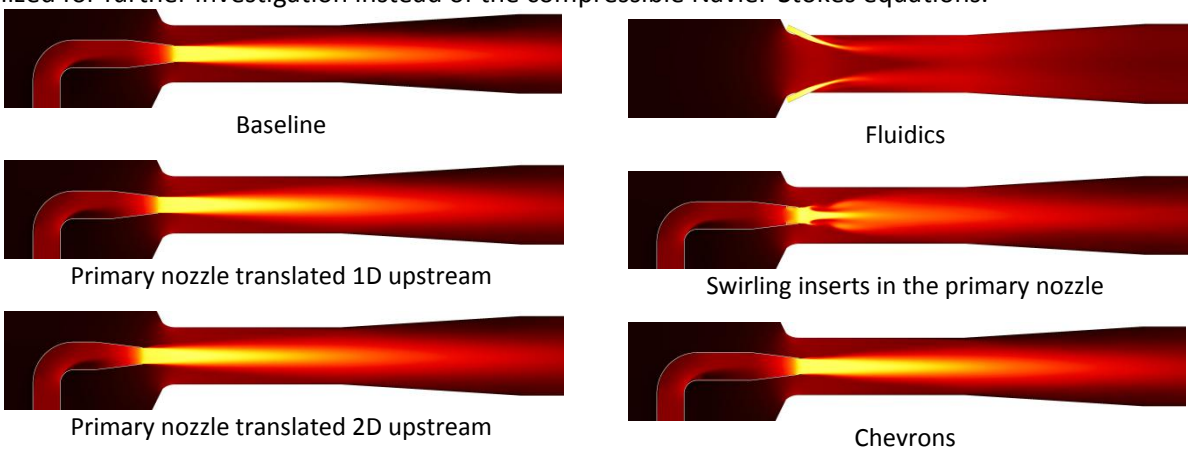

Figure 381. The time-averaged Mach number contours for the different cases are shown.

The coherent flow structure can be defined by different means, while a clear definition accepted by the entire fluid dynamic community does not exist. This lead to the development of various proposed modal decomposition methods to visualize coherent structures in the flow, as e.g. Fourier mode decomposition, Proper Orthogonal Decomposition (POD), or Dynamic Mode Decomposition (DMD). Each of these flow decomposition methods has been designed for a certain purposes, where it can be advantageous.
An often employed method in engineering applications is the POD method. The identification criterion for coherence of the flow structures is the correlation of the instantaneous velocity samples. Since the velocity is thereby multiplied, the result can be interpreted as a dynamic pressure or flow energy weighting in the incompressible case. Further, all computed spatial modes are orthogonal to each other.
A further purpose of the method is the low-order modeling of the fluid dynamic process in a certain application. The formulation of the method provides that such a low-order modeling contains the

optimal amount of flow energy by a sum of modes.
For acoustic purposes, spectral decomposition method is preferred, where desecrate frequencies are distinguishable, since each frequency can be investigated independently. With the DMD method, the modes are computed spectrally exclusive or orthogonal. Additionally, the DMD method provides a growth rate of the mode.
For an initial analysis of the high frequency spectra of the flow-field, 2178 individual time instants have been acquired at a sampling rate of 312.5 kHz (corresponding to a sampling every 3.2·10-6 s). Hence, a frequency range of about 144 Hz to 156,250 Hz is covered in this analysis.
The spectra of the pressure DMD analysis consists of a low frequency lobe at the low frequencies and five high frequency peaks, as shown in Figure 39. Each peak is represented by a couple of modes, where each individual mode is indicated by a black ring symbol in Figure 39. The first five pressure modes with the highest mode magnitude are associated with the shedding downstream of the jet pipe outlet, which occurs at a frequency of 36.09 kHz. The following modes in magnitude rank are associated with low frequency flow phenomena taking place in the jet pump. Due to the frequency discretization of the spectra by the sampled modes and the averaging over the entire investigation domain, the lower frequency peaks are hardly distinguishable.

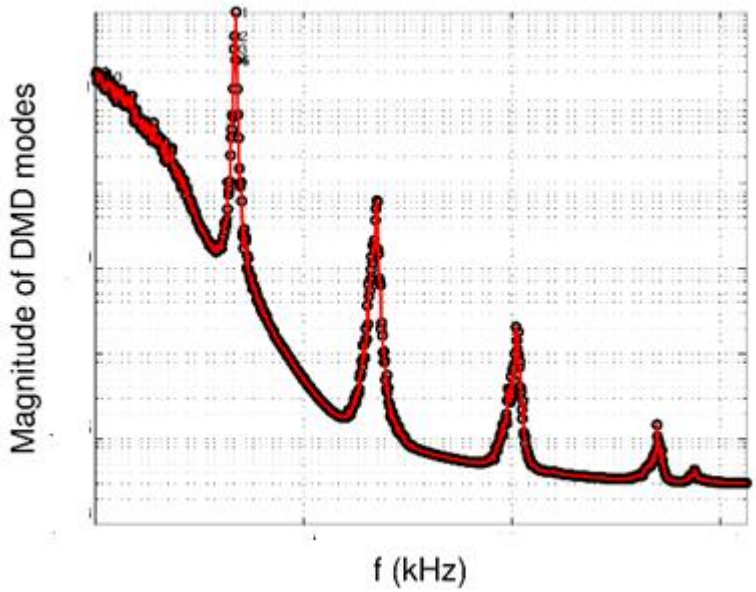

Figure 39. The normalized power spectra density of the static pressure modes.

The growth rate of the computed modes is shown in Figure 40, where the high amplitude modes are colored accordingly to the amplitude in shades of red (high amplitude in red to low amplitude in white). An apparent feature of the flow is that the high frequency modes exhibit a larger growth rate than the low frequency modes. However, the highest frequent modes exhibit a very low magnitude, as shown in Figure 39. Therefore, the consequence of these flow modes onto the flow-field development is minor. The mode with the highest amplitude has a negative growth rate, which indicates that the mode is decaying over time. However, the second, fourth, and fifth mode have a slight negative growth rate and growth therefore over time.
Thus, the empirical Ritz eigenvalues are shown in Figure 41 and it can be observed that all eigenvalues lay perfectly on the unit cycle.
Three examples of pressure DMD mode shapes are shown in Figure 42, for the entire investigated domain by the modal decomposition. The mode shown in Figure 42 (a) exhibits the highest amplitude of all modes and is associated with the frequency of 36.09 kHz. The mode shape clearly reveals the high

frequency acoustic wave propagation downstream of the primary pipe exit. Further, the extent of the high amplitude frequency waves in the domain is visible and the interaction at the shear layer can be seen. The other four high amplitude modes associated with the shedding frequency peak exhibit a generally similar topological shape. However, the peak value in the mode topology changes location around the primary pipe exit for the different modes, indicating that wave frequency slightly changes around the primary pipe exit due to the slight difference of the velocity inside the primary pipe.

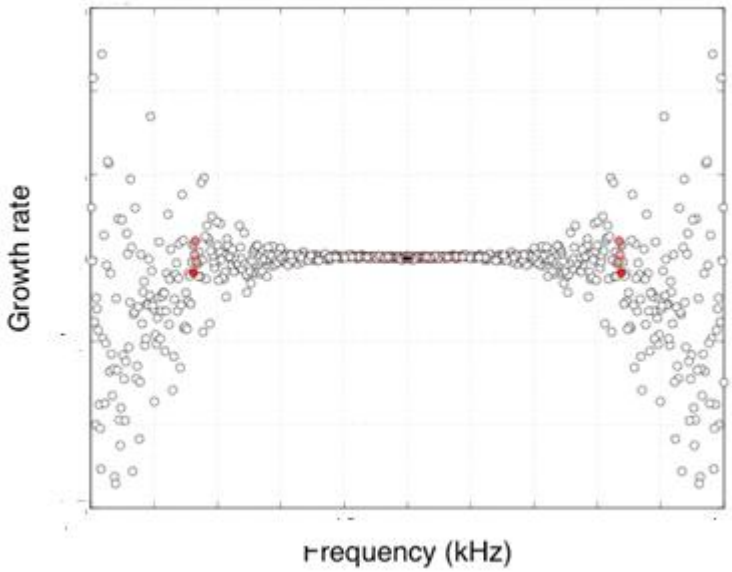

Figure 40. The growth rate of the dynamic mode decomposition modes. High amplitude modes in red.

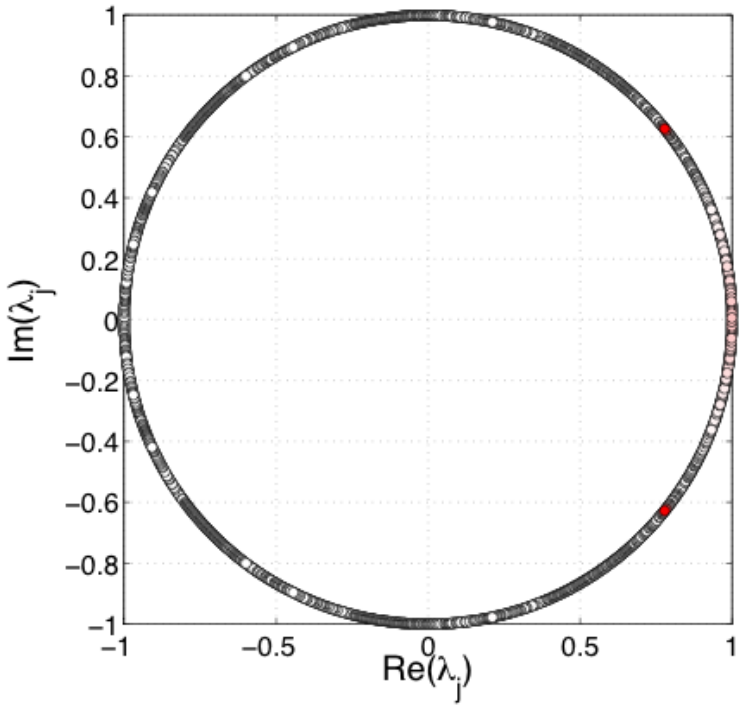

Figure 41. The empirical Ritz eigenvalues.

The mode shapes shown in Figure 42 (b) and (c) are associated with the hydrodynamic flow motion at the low frequencies of some kHz occurring in the mixing channel, and correspond to the 19th and the 6th mode in the amplitude ranking, respectively. However, the analysis does not reveal a high enough

temporal resolution in order to distinguish detailed flow phenomena in the low frequency range. Thus, the modes correspond rather to frequency ranges than to discrete frequencies. The 6th pressure DMD mode is associated to the lower frequency range captured and exhibits high values in the transition region between the straight mixing channel and the diffuser section. The azimuthal mode shapes describe the propagation of the disk-like structures generated some distance downstream from the primary pipe exit, which spread in radial direction while moving downstream. The mode structures interact with the mixing channel wall boundary layer and might be responsible for the boundary layer separation, which is observed at this location. Worthwhile to note is that the modal structure shapes remain until the outlet of the jet pump.

The 19th pressure DMD mode has higher frequency content than the 6th mode shown. The mode is initiated further upstream than previously low frequency described mode, where the mode shape exhibits the highest amplitudes. For both low frequency associated modes, slightly altered magnitudes arising from the inside of the primary pipe are notable. Thus, these disturbance frequencies coming from inside the primary pipe might be intensified in the shear layer due to its receptivity. The mode shape describes the unsteady flow transition, which is prolonged far into the diffuser region. However, the modal shape exhibits a significant decrease of the magnitudes towards the outlet of the jet pump.

In Figure 42, the plane represents a longitudinal mid-plane cut and the primary pipe bend is positioned towards the top. The color scale is chosen such that the general modal shape becomes illustrative.

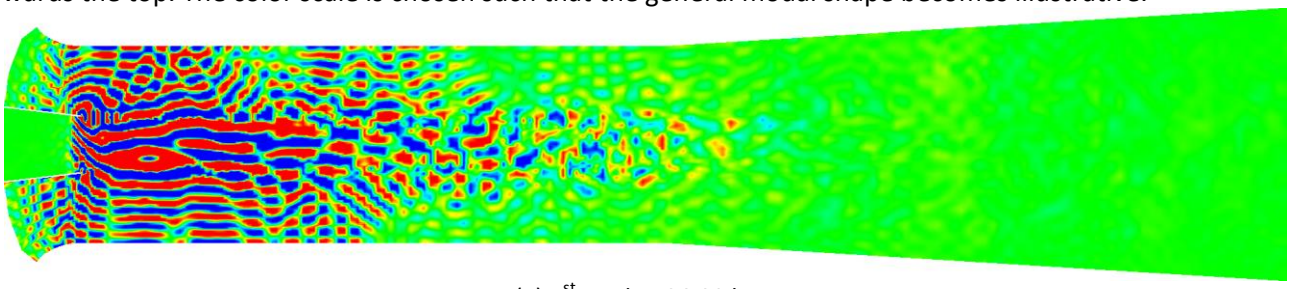

(a) 1st mode - 36.09 kHz

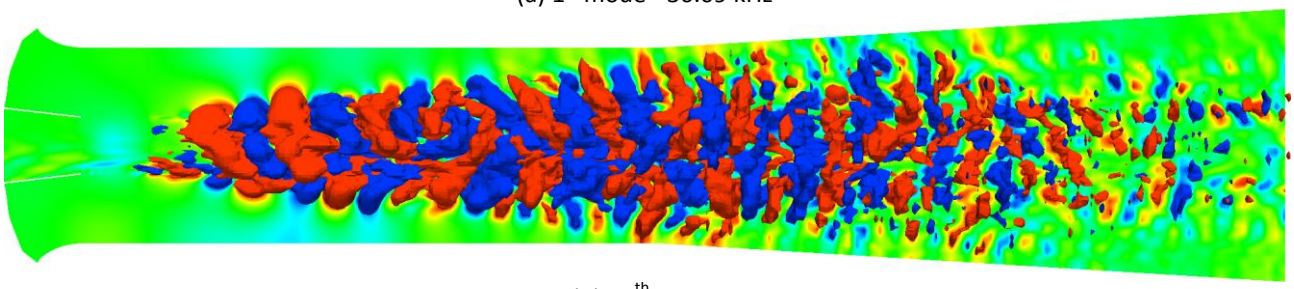

(b) 19th mode

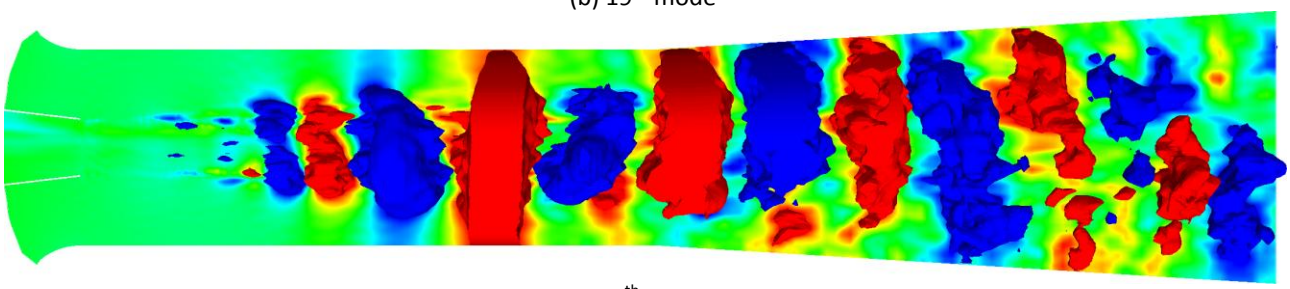

(c) 6th mode

Figure 42. Three DMD pressure modes corresponding to high frequency (a) and low frequency phenomena (b) and (c).

The numerical data was compared to experimental flow visualisations in the mixing channel of the jet pump. PIV measurements are a challenging task at high flow speeds especially in confined environment, which does not allow free access to the flow field. Figure 43 shows for the baseline configuration the ensemble averaged streamwise velocity data measured experimentally over-plotted on the numerical data for a number of radial lines. The streamwise velocity magnitudes from the experiments at the centreline of the jet are in agreement with the numerical data. Nonetheless, higher flow velocities are predicted outside of the jet plume with the experimental approach as well as towards the walls of the configuration where the lower velocity secondary flow is present. This might be caused by reflections at the pipe walls. Light refraction causes that high velocities are observed over the entire channel width and only the velocities around the centreline are useable.

The sound pressure levels received in the far field were evaluated numerically and experimentally, where the comparison for different radiation angles is illustrated in Figure 44 (sound pressure levels as function of directivity angles). The acoustic noise radiation is dominant at the downstream angles between 145° and 160°, which is consistently observed for all configurations. This acoustic noise directivity is typical for large-scale turbulent mixing noise. Note that in both experimental and numerical calculations the trends are similar. When moving the primary nozzle upstream, the acoustic noise at the jet pump exit is reduced compared to the baseline. Moreover, with fluidic injection from the mixing channel walls, the acoustic noise emission can be significantly further reduced. These trend observations are in agreement when considering both the numerical and experimental methods.

However, the sound pressure levels are experimentally measured to be higher compared to the numerical estimation. This might be caused by several factors as described here. First, the numerical grid was designed such that the entire domain is covered by one simulation. The flow speeds are locally high at the primary nozzle exit, which requires small time steps. Due to the different velocity scales at the jet pump exit as compared with the primary nozzle exit, small time steps are performed in the entire domain. This represents a substantial numerical effort. More simulation time would be required to capture accurately the low frequency characteristics of the acoustic noise in order to compare the frequency spectra between the simulations and experiments in a reasonable manner. The unresolved low-frequency content might be one reason for the discrepancies between the numerical and experimental results observed in Figure 44. Longer simulation time could clarify this issue. Another outcome with the set-up is that the mesh grid is relatively coarse towards the far-field, outside and downstream of the jet pump exit. This is in order to keep the total numerical afford in reasonable limits. This might cause numerical dissipation effects leading to lower pressure fluctuation intensities emitted into far field. Another aspect with the present simulations is that any noise radiation due to the aero-vibro-acoustics phenomena involving the interaction between the flow and the inner jet-pump structure are neglected.

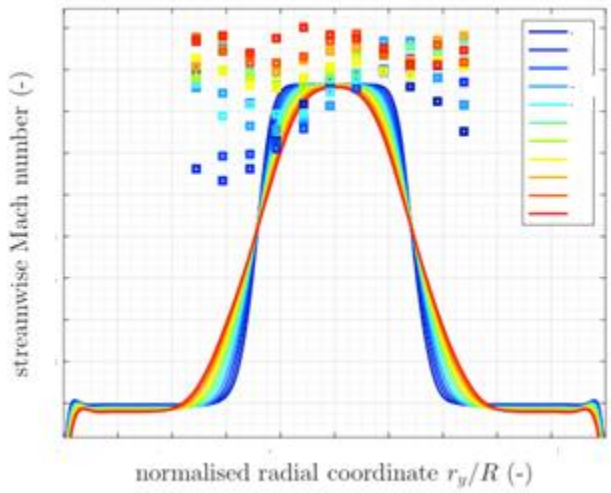

Figure 43. Radial profiles of the stream wise Mach number

Nonetheless, a qualitative good agreement could be achieved between the simulations and the experimental data. The predicted differences between the cases were in good agreement to the experiments.

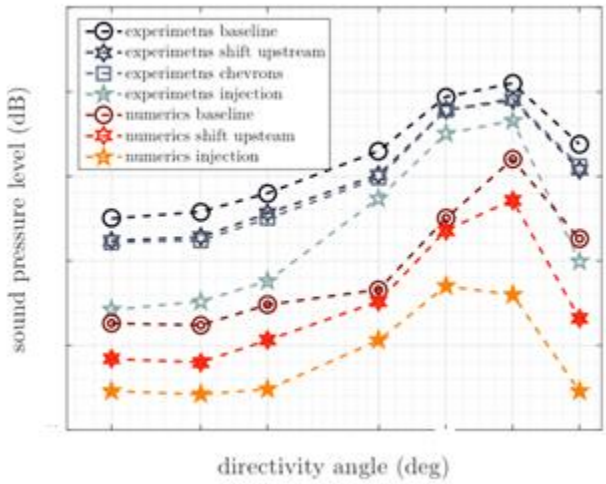

Figure 44. Experimental and numerical results evaluating the acoustic noise